

# Search for the metal-weak thick disk from the LAMOST DR5

T.-S. Yan<sup>1,2</sup>, J.-R. Shi<sup>1,2</sup>, H. Tian<sup>3</sup>, W. Zhang<sup>1</sup> and B. Zhang<sup>4</sup>

<sup>1</sup> Key Laboratory of Optical Astronomy, National Astronomical Observatories, Chinese Academy of Sciences, Beijing 100012, China; *sjr@bao.ac.cn*

<sup>2</sup> School of Astronomy and Space Science, University of Chinese Academy of Sciences, Beijing 100049, China

<sup>3</sup> Key Laboratory of Space Astronomy and Technology, National Astronomical Observatories, Chinese Academy of Sciences, Beijing 100101, People's Republic of China; *tianhao@nao.cas.cn*

<sup>4</sup> Department of Astronomy, Beijing Normal University, Beijing 100875, China

**Abstract** Based on the data release of the Large Sky Area Multi-Object Fiber Spectroscopic Telescope survey (LAMOST DR5) and the *Gaia* Early Data Release 3 (*Gaia* EDR3), we construct a sample containing 46,109 giant ( $\log g \leq 3.5$  dex) stars with heliocentric distance  $d \leq 4$  kpc, and the sample is further divided into two groups of the inner ( $R_{GC} < 8.34$  kpc) and outer region ( $R_{GC} > 8.34$  kpc). The  $L_Z$  distributions of our program stars in the panels with different  $[Fe/H]$  and  $[\alpha/Fe]$  suggest that the thick-disk consists of two distinct components with different chemical compositions and kinematic properties. For the inner region, the metal-weak thick disk (MWTD) contributes significantly when  $[\alpha/Fe] > +0.2$  dex and  $[Fe/H] < -0.8$  dex, while the canonical thick-disk (TD) dominates when  $[Fe/H] > -0.8$  dex. However, MWTD clearly appears only when  $[\alpha/Fe] > +0.2$  dex and  $[Fe/H] < -1.2$  dex for the outer region, and its proportion is lower than that of the inner region within the same metallicity. Similar result can be obtained from the  $V_\phi$  distribution. The high fraction of MWTD in the inner than that in the outer region imply that MWTD may form in the inner disk, **and is an observational evidence about the inside-out disk formation scenario.**

**Key words:** stars: abundances – stars: atmospheres – Galaxy: structure – Galaxy: kinematics and dynamics – methods: data analysis

## 1 INTRODUCTION

It is well known that the Milky Way is composed of multiple components, such as the thin-disk, the thick-disk and the halo (An & Beers, 2020; Chiappini et al., 1997; van der Kruit & Freeman, 2011), and it provides a unique chance for studying the formation and evolution of galaxies in detail by analysing the full location, kinematics characteristic and chemical compositions of these stellar components.

As an important component of our Galaxy, the thick-disk has been studied by numerous works since its discovery (Beraldo e Silva et al., 2021; Di Matteo et al., 2011, 2019; Franchini et al., 2021; Gilmore & Reid, 1983; Girard et al., 2006; Helmi et al., 2018; Recio-Blanco et al., 2014; Ruchti et al., 2011). The thick-disk is composed primarily of older stars, resulting in different chemical composition from the young thin-disk stars. In the metallicity distribution, the thick-disk exhibits a peak around  $[Fe/H] \sim -0.6$  dex, and most of the thick-disk stars fall within the interval of  $[Fe/H]$  from  $-1.0$  dex to  $-0.3$  dex (Reddy & Lambert, 2008). At the mooment, there is no uniform conclusion on the upper

and lower bounds of the metallicity distribution for the thick-disk stars (Reddy & Lambert, 2008), and some disk-like kinematics stars with very low metallicity (down to  $[\text{Fe}/\text{H}] = -1.7$  dex, or even lower) have been found (Carollo et al., 2010, 2019; Chiba & Beers, 2000; Norris et al., 1985). These metal-poor tail stars are commonly considered belong to the metal-weak thick-disk (MWTD, Beers et al., 2014; Carollo et al., 2010, 2019; Carollo & Chiba, 2020; Ivezić et al., 2008; Morrison et al., 1990; Reddy & Lambert, 2008; Ruchti et al., 2011), while the remaining component after removing MWTD from the thick-disk is called as the canonical thick-disk (TD, Carollo et al., 2010).

Due to lack of large-scale sample stars of high-precision parameters, the existence of MWTD remains controversial (Ruchti et al., 2010). Norris et al. (1985) suggested that these stars with  $[\text{Fe}/\text{H}] \leq -1.0$  dex and  $e \leq 0.4$  should belong to a population, and Morrison et al. (1990) referred to these stars of  $-1.6 \text{ dex} < [\text{Fe}/\text{H}] < -1.0 \text{ dex}$  with kinematical and spatial properties similar to the thick-disk ones as MWTD stars. It need to be pointed out that the metallicity derived by Norris et al. (1985) and Morrison et al. (1990) is based on the information from the David Dunlap Observatory (DDO) photometry, and Twarog & Anthony-Twarog (1994) found that the photometric metallicity used by Norris et al. (1985) has an  $\sim 0.5$  dex offset from the spectral ones for giants near  $[\text{Fe}/\text{H}] \sim -1.2$  dex. In addition, by comparing the metallicity obtained from the high-resolution spectra with these from the DDO photometry for giants of Norris et al. (1985) and Morrison et al. (1990), Ryan & Lambert (1995) concluded that most stars with the DDO photometric metallicity of  $[\text{Fe}/\text{H}] < -1.0$  dex have spectral metallicities of  $[\text{Fe}/\text{H}] > -1.0$  dex. As a result, these stars identified as belonging to MWTD by Norris et al. (1985) and Morrison et al. (1990), therefore should belong to TD. Although the conclusions from Twarog & Anthony-Twarog (1994) and Ryan & Lambert (1995) cannot rule out the existence of MWTD, the evidences of MWTD suggested by Norris et al. (1985) and Morrison et al. (1990) become weaker.

Fortunately, the advent of large-scale surveys, such as the Large Sky Area Multi-Object Fibre Spectroscopic Telescope (LAMOST) survey (Cui et al., 2012), the Sloan Digital Sky Survey (SDSS, York et al., 2000), the Radial Velocity Experiment spectroscopic survey (RAVE, Steinmetz et al., 2020a,b), and the *Gaia* mission (Gaia Collaboration et al., 2021), make it possible to perform accurate chemodynamical studies on the stellar populations in our Galaxy (Carollo et al., 2019). The spectra from LAMOST, SDSS and RAVE provide estimation of the stellar atmospheric parameters (effective temperature, surface gravity and metallicity) and radial velocities (RV), and the *Gaia* satellite delivers high-precision astrometric data (position, trigonometric parallax, and proper motions). The combination of parameters obtained from spectrum and astrometry is a powerful tool for studying the properties of stellar component related to the Milky Way by investigating the perspectives of stellar spatial distribution, chemical composition and kinematics.

In this paper, based on a sample combining spectral information from LAMOST and astrometric data from *Gaia*, we examine MWTD. The paper is organized as follows. In Sect. 2, we describe the selection of our sample stars. Sect. 3 presents the search for MWTD in the kinematic space, and the discussion and conclusions are given in Sect. 4.

## 2 SAMPLE

### 2.1 Selection of the Sample Stars

The sample stars are selected from LAMOST DR5 with a range of the effective temperature from 4,500 K to 7,000 K, and only the giants ( $\log g \leq 3.5$  dex) with signal-to-noise (S/N) ratio of their spectra higher than 50 have been considered. This removes all the dwarf stars. The stellar atmosphere parameters and  $[\alpha/\text{Fe}]$  ratios are taken from the recommended values of Xiang et al. (2019) with internal uncertainties of  $[\text{Fe}/\text{H}]$  and  $[\alpha/\text{Fe}]$  less than 0.07 and 0.05 dex, respectively, while, the radial velocities (RVs) are adopted from LAMOST DR5 (Luo et al., 2015), and only the objects with a RV uncertainty less than  $10 \text{ km s}^{-1}$  have been selected. Moreover, to further ensure the accuracy of the metallicity, only the objects with a difference of metallicity between LAMOST DR5 and that of Xiang et al. (2019) less than 0.1 dex are selected.

The stellar proper motions (PMs) are obtained from *Gaia* EDR3 (Gaia Collaboration et al., 2021) with errors both in right ascension and in declination direction less than  $0.2 \text{ mas yr}^{-1}$ , while the geometric distances ( $r_{\text{med}}$ ) from Bailer-Jones et al. (2021) have been adopted. Our sample stars are confined to  $d \leq 4 \text{ kpc}$  with an uncertainty of  $(r_{\text{hi}} - r_{\text{lo}})/(2 \times r_{\text{med}})$  smaller than 20%. Here,  $r_{\text{lo}}$  and  $r_{\text{hi}}$  are the 16th and 84th percentiles of the posterior (see Bailer-Jones et al., 2021, for details).

After these considerations included, the number of stars is reduced to 211,046, and the distribution of these stars in the  $[\alpha/\text{Fe}]$  -  $[\text{Fe}/\text{H}]$  plane is shown in Fig. 1. Obviously, most of them are belong to the thin-disk, and these thin-disk stars are not important for this study. Therefore, according to the criteria of Hayden et al. (2014) (see the black yellow polyline in Fig. 1) we remove them from our sample. Finally, there are 46,109 stars in our sample.

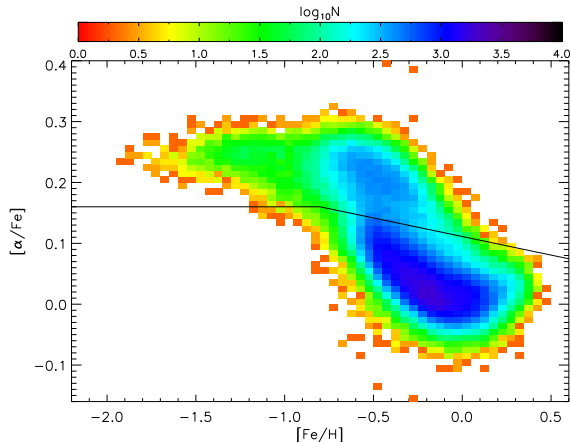


Fig. 1: Distribution of giant stars in the  $[\alpha/\text{Fe}]$  -  $[\text{Fe}/\text{H}]$  plane. The black yellow polyline is the criteria for dividing the thin- and thick-disk stars from Hayden et al. (2014).

To avoid the systematic offset of LAMOST RVs (Anguiano et al., 2018; Tian et al., 2020), we compare the LAMOST RVs with those from *Gaia* EDR3 for the common stars, only stars with *Gaia* RV errors less than  $1 \text{ km s}^{-1}$  have been selected. The offset of LAMOST RV is around  $-4.85 \text{ km s}^{-1}$  (Fig. 2), which is very close to those of the previous works ( $\sim -5 \text{ km s}^{-1}$ , Anguiano et al., 2018; Tian et al., 2020). Therefore, a value of  $4.85 \text{ km s}^{-1}$  is added to the LAMOST RV to compensate for the offset.

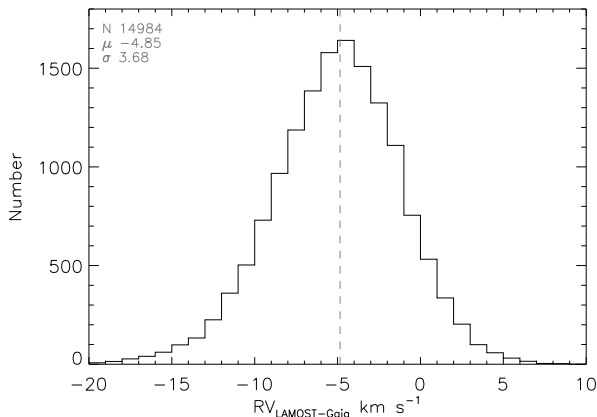


Fig. 2: Comparison of the LAMOST RVs with those from *Gaia* EDR3, only stars with *Gaia* RV errors less than  $1 \text{ km s}^{-1}$  have been used.

## 2.2 Stellar Kinematic Parameters

The full phase-space information, positions (including  $\alpha$ ,  $\delta$  and  $l$ ,  $b$ ), PMs and distances, combined with RVs, provide the parameters required to calculate the kinematics. Following Kordopatis et al. (2011), the Galactic-centered Cartesian coordinates  $(X_{GC}, Y_{GC}, Z)$  of stars are obtained through their distances and Galactic coordinates ( $l$ ,  $b$ ), and  $R_{GC} = \sqrt{X_{GC}^2 + Y_{GC}^2}$  represents the distance to the Galactic center in planar radial coordinate. In our calculation, the solar position of  $(X_{\odot}, Y_{\odot}, Z_{\odot}) = (8.34 \text{ kpc}, 0, 0)$  is adopted (Reid et al., 2014). The galactocentric velocities  $V_R$  and  $V_{\phi}$  are also calculated, and  $V_R$  and  $V_{\phi}$  are defined as positive with increasing  $R_{GC}$  and  $\phi$ , respectively. The Galactic rotation velocity of the Local Standard of Rest (LSR) is adopted as  $V_c = 240 \text{ km s}^{-1}$  (Reid et al., 2014), and the solar motion with respect to LSR of  $(U_{\odot}, V_{\odot}, W_{\odot}) = (11.1, 12.24, 7.25) \text{ km s}^{-1}$ , is taken from Schönrich et al. (2010). The Z-axis angular momentum is derived using the relationship of  $L_Z = R_{GC} \times V_{\phi}$ .

## 3 RESULTS

Although MWTD overlaps TD and the halo in parameter space, it is still possible to trace the footprint of MWTD with the help of their distribution in the metallicities, kinematics and dynamics (An & Beers, 2020, 2021; Carollo et al., 2010, 2019; Carollo & Chiba, 2020; Cordoni et al., 2021; Kordopatis et al., 2013).

It is noted that the fraction of metal-poor stars is lower (see Fig. 8 of Miranda et al., 2016), and Carollo et al. (2010) pointed out that the significant contribution of MWTD is within  $-1.8 \text{ dex} < [\text{Fe}/\text{H}] < -0.8 \text{ dex}$ , and possibly up to  $\sim -0.7 \text{ dex}$ . Therefore, we divide our sample stars into four metallicity intervals of  $[\text{Fe}/\text{H}] < -1.2 \text{ dex}$ ,  $-1.2 \text{ dex} < [\text{Fe}/\text{H}] < -0.8 \text{ dex}$ ,  $-0.8 \text{ dex} < [\text{Fe}/\text{H}] < -0.4 \text{ dex}$  and  $[\text{Fe}/\text{H}] > -0.4 \text{ dex}$ . Moreover, Carollo et al. (2019) suggested that the MWTD stars tend to have higher  $[\alpha/\text{Fe}]$  ratios than those of TD, which means it will improve the search efficiency of MWTD when the sample is decomposed in  $[\alpha/\text{Fe}]$  space. In Fig. 3 we plot the  $[\alpha/\text{Fe}]$  distribution of our sample stars of  $[\text{Fe}/\text{H}] < -0.8 \text{ dex}$ , and the distribution can be well fitted with two Gaussian functions. According to their  $[\alpha/\text{Fe}]$  distribution, the sample is further divided into high ( $[\alpha/\text{Fe}] > +0.2 \text{ dex}$ ) and low  $\alpha$  ( $[\alpha/\text{Fe}] < +0.2 \text{ dex}$ ) intervals.

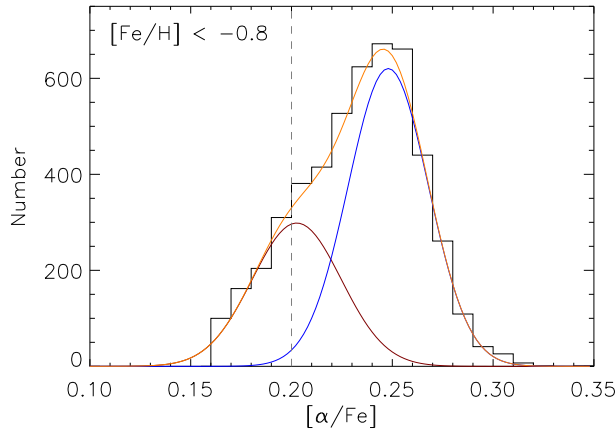


Fig. 3:  $[\alpha/\text{Fe}]$  distribution of the sample stars with  $[\text{Fe}/\text{H}] < -0.8 \text{ dex}$ . The distribution can be well fitted with two Gaussian components. The vertical dotted line is labeled as  $[\alpha/\text{Fe}] = +0.2 \text{ dex}$ .

In order to compare the differences due to different  $R_{GC}$  (e.g., An & Beers, 2021), we present our discussions on our program stars with the inner ( $R_{GC} < 8.34$ , 23,664 stars) and outer ( $R_{GC} > 8.34 \text{ kpc}$ , 22,445 stars) regions.

Table 1: The parameters of the best-fit components in the  $L_Z$  distributions for the inner region stars in slices of  $[\text{Fe}/\text{H}]$  and  $[\alpha/\text{Fe}]$ . The units of the  $L_Z$  peak and scatter ( $\sigma_{LZ}$ ) are in  $\text{kpc km s}^{-1}$ .

$[\alpha/\text{Fe}]$ Component	$[\text{Fe}/\text{H}] < -1.2 \text{ dex}$			$-1.2 \text{ dex} < [\text{Fe}/\text{H}] < -0.8 \text{ dex}$			$-0.8 \text{ dex} < [\text{Fe}/\text{H}] < -0.4 \text{ dex}$			$[\text{Fe}/\text{H}] > -0.4 \text{ dex}$		
	fraction	$L_Z$ peak	$\sigma_{LZ}$	fraction	$L_Z$ peak	$\sigma_{LZ}$	fraction	$L_Z$ peak	$\sigma_{LZ}$	fraction	$L_Z$ peak	$\sigma_{LZ}$
$> 0.2$ TD				0.40 $\pm$ 0	1253.5 $\pm$ 11.3	391.6 $\pm$ 26.4	0.89 $\pm$ 0	1328.2 $\pm$ 7.1	346.1 $\pm$ 5.0	1.00 $\pm$ 0	1412.0 $\pm$ 8.0	341.3 $\pm$ 5.9
MWTD	0.35 $\pm$ 0	950.7 $\pm$ 7.0	444.9 $\pm$ 35.4	0.39 $\pm$ 0.08	948.5 $\pm$ 11.2	527.5 $\pm$ 37.0						
the halo	0.65 $\pm$ 0.03	-0.2 $\pm$ 7.1	733.6 $\pm$ 33.6	0.21 $\pm$ 0.02	1.8 $\pm$ 11.2	508.8 $\pm$ 31.5	0.11 $\pm$ 0.01	391.6 $\pm$ 41.5	405.2 $\pm$ 18.8			
$< 0.2$ TD				0.67 $\pm$ 0	1265.3 $\pm$ 40.8	390.0 $\pm$ 33.7	0.94 $\pm$ 0	1383.1 $\pm$ 7.2	356.2 $\pm$ 5.5	1.00 $\pm$ 0	1464.0 $\pm$ 4.5	331.6 $\pm$ 3.3
the halo				0.33 $\pm$ 0.05	91.2 $\pm$ 61.4	490.6 $\pm$ 50.1	0.06 $\pm$ 0.01	329.6 $\pm$ 48.1	384.9 $\pm$ 23.8			

### 3.1 The $L_Z$ distributions

Following Carollo et al. (2019), we focus on the  $L_Z$  distribution. In Fig. 4, we plot the  $L_Z$  distribution for the inner region stars ( $R_{GC} < 8.34$ ) in slices of  $[\text{Fe}/\text{H}]$  and  $[\alpha/\text{Fe}]$ . We apply multi-Gaussians to fit the  $L_Z$  distribution in each panel, and the fitting parameters of each component including the fraction,  $L_Z$  and scatter ( $\sigma_{LZ}$ ) are derived according to the Bayesian method, which can effectively avoid the contamination between different components (Tian et al., 2019). To perform this fitting, we apply *emcee* (Foreman-Mackey et al., 2013) to run a Markov Chain Monte Carlo (MCMC) simulation. We use 100 walkers for 2000 iterations with 1000 burn-in have been used. The median value for each parameter is adopted, and the difference between the median value and the 16% and 84% values are used as the upper and lower uncertainties, respectively. Fig 5 shows the MCMC result of panel b in Fig. 4.

The best-fit parameters and uncertainties of the MCMC simulations for all the subsamples are listed in Table 1. When the fraction is not a free parameter during the MCMC simulation (one in each panel), its uncertainty is marked as 0 (Table 1). The fitted distributions are represented with brown, red, green and blue lines for the halo, MWTD, TD and total, respectively, in Fig. 4.

It can be seen from Fig. 4 that the three low  $\alpha$  ( $[\alpha/\text{Fe}] < +0.20 \text{ dex}$ ) panels (f, g and h) are dominated by the TD stars, and their  $L_Z$  peaks gradually decrease with decreasing metallicity. When  $[\text{Fe}/\text{H}] < -0.4 \text{ dex}$ , the halo exists (panels f and g), and it accounts for about one third when  $-1.2 \text{ dex} < [\text{Fe}/\text{H}] < -0.8 \text{ dex}$  (panel f).

For the four high  $\alpha$  panels, the  $L_Z$  distributions vary regularly with the metallicity. The TD stars dominate both in panels c and d, and the  $L_Z$  distribution of these two panels are very similar to those of panels g and h. The typical  $L_Z$  peak value is around  $1350 \text{ kpc km s}^{-1}$ .

We note that there are three components in panel b, and one of them has a  $L_Z$  peak of  $948.5 \pm 11.2 \text{ kpc km s}^{-1}$  with a scatter of  $527.5 \pm 37.0 \text{ kpc km s}^{-1}$ , this value is lower than that of TD ( $1253.5 \pm 11.3 \text{ kpc km s}^{-1}$ ), while, it is higher than that of the halo ( $1.8 \pm 11.2 \text{ kpc km s}^{-1}$ ). Which indicates that this component is dynamically different from those of the halo and TD, and it is most likely to be MWTD (An & Beers, 2020; Carollo et al., 2010; Naidu et al., 2020). The difference of the  $L_Z$  peak between MWTD and TD is around  $300 \text{ kpc km s}^{-1}$ , which is larger than that of the fitting error. Our results present that the fraction of MWTD in this panel is around 0.39, while the fractions of the halo and TD are  $\sim 0.21$  and  $\sim 0.40$ , respectively.

For the more metal-poor panel a, although there are only two components, we notice that there is a component with a  $L_Z$  peak of  $950.7 \pm 7.0 \text{ kpc km s}^{-1}$  with a scatter of  $444.9 \pm 35.4 \text{ kpc km s}^{-1}$ . This  $L_Z$  peak value is very close to that of MWTD in panel b, which indicates this component is also MWTD. The contribution of MWTD in this panel is about one third (0.35). The remaining contribution in the panel accounts for about two-thirds, and they comes from the halo of a  $L_Z$  peak of  $-0.2 \pm 7.1 \text{ kpc km s}^{-1}$  with a sccter of  $733.6 \pm 33.6 \text{ kpc km s}^{-1}$ .

Fig. 6 presents the  $L_Z$  distributions of the outer region stars ( $R_{GC} > 8.34 \text{ kpc}$ , black histogram) in slices of  $[\text{Fe}/\text{H}]$  and  $[\alpha/\text{Fe}]$ . Similar to the inner region, we apply *emcee* to perform a MCMC simulation to determine the components contained of each panel for the outer region stars. The best-fit components obtained through the simulation are superimposed on the histogram of Fig. 6 with color curves, and the best-fit parameters are listed in Table 2.

Table 2: Similar to Table 1, but for the outer region stars.

[ $\alpha$ /Fe] Component	[Fe/H] < -1.2			-1.2 < [Fe/H] < -0.8			-0.8 < [Fe/H] < -0.4			[Fe/H] > -0.4		
	fraction	$L_Z$ peak	$\sigma_{LZ}$	fraction	$L_Z$ peak	$\sigma_{LZ}$	fraction	$L_Z$ peak	$\sigma_{LZ}$	fraction	$L_Z$ peak	$\sigma_{LZ}$
> 0.2				0.72 $\pm$ 0	1432.5 $\pm$ 12.8	475.6 $\pm$ 15.0	0.91 $\pm$ 0	1600.4 $\pm$ 10.5	386.8 $\pm$ 6.4	1.00 $\pm$ 0	1697.4 $\pm$ 10.2	378.7 $\pm$ 7.3
	TD											
	MWTD	0.24 $\pm$ 0	996.9 $\pm$ 22.0	687.8 $\pm$ 62.1								
	the halo	0.76 $\pm$ 0.04	60.8 $\pm$ 21.9	701.4 $\pm$ 30.2	0.28 $\pm$ 0.02	19.1 $\pm$ 15.2	555.4 $\pm$ 28.1	0.09 $\pm$ 0.02	625.3 $\pm$ 136.6	494.0 $\pm$ 55.2		
< 0.2				0.59 $\pm$ 0	1736.4 $\pm$ 44.1	427.2 $\pm$ 30.1	0.96 $\pm$ 0	1779.6 $\pm$ 49.8	427.9 $\pm$ 14.2	1.00 $\pm$ 0	1808.0 $\pm$ 4.8	350.2 $\pm$ 3.4
	TD											
	the halo			0.41 $\pm$ 0.04	211.3 $\pm$ 86.7	525.5 $\pm$ 62.6	0.04 $\pm$ 0.01	450.4 $\pm$ 30.1	485.2 $\pm$ 35.8			

Table 3: The parameters of the best-fit components in the  $V_\phi$  distributions for inner region stars ( $R_{GC} < 8.34$  kpc). The units of  $\langle V_\phi \rangle$  and  $\sigma_{V_\phi}$  are in  $\text{km s}^{-1}$ .

[ $\alpha$ /Fe] Component	[Fe/H] < -1.2			-1.2 < [Fe/H] < -0.8			-0.8 < [Fe/H] < -0.4			[Fe/H] > -0.4		
	fraction	$V_\phi$ peak	$\sigma_{V_\phi}$	fraction	$V_\phi$ peak	$\sigma_{V_\phi}$	fraction	$V_\phi$ peak	$\sigma_{V_\phi}$	fraction	$V_\phi$ peak	$\sigma_{V_\phi}$
> 0.2				0.38 $\pm$ 0	177.4 $\pm$ 7.2	47.6 $\pm$ 3.9	0.88 $\pm$ 0	176.5 $\pm$ 0.9	43.6 $\pm$ 0.6	1.00 $\pm$ 0	183.7 $\pm$ 1.0	42.9 $\pm$ 0.7
	TD											
	MWTD	0.35 $\pm$ 0	124.9 $\pm$ 6.3	63.4 $\pm$ 6.5	0.40 $\pm$ 0.12	117.8 $\pm$ 10.7	64.6 $\pm$ 8.8					
	the halo	0.65 $\pm$ 0.05	1.4 $\pm$ 6.8	101.6 $\pm$ 5.5	0.22 $\pm$ 0.05	6.2 $\pm$ 10.6	71.2 $\pm$ 6.2	0.12 $\pm$ 0.01	57.8 $\pm$ 6.0	55.9 $\pm$ 2.6		
< 0.2				0.54 $\pm$ 0	181.5 $\pm$ 6.4	42.0 $\pm$ 5.3	0.92 $\pm$ 0	185.0 $\pm$ 0.9	43.0 $\pm$ 0.7	1.00 $\pm$ 0	190.2 $\pm$ 0.5	40.4 $\pm$ 0.4
	TD											
	the halo			0.46 $\pm$ 0.08	43.3 $\pm$ 14.9	77.4 $\pm$ 8.2	0.08 $\pm$ 0.01	54.6 $\pm$ 6.4	53.7 $\pm$ 3.1			

Table 4: Similar to Table 3 but for the  $V_\phi$  distributions of outer region stars ( $R_{GC} > 8.34$  kpc).

[ $\alpha$ /Fe] Component	[Fe/H] < -1.2			-1.2 < [Fe/H] < -0.8			-0.8 < [Fe/H] < -0.4			[Fe/H] > -0.4		
	fraction	$V_\phi$ peak	$\sigma_{V_\phi}$	fraction	$V_\phi$ peak	$\sigma_{V_\phi}$	fraction	$V_\phi$ peak	$\sigma_{V_\phi}$	fraction	$V_\phi$ peak	$\sigma_{V_\phi}$
> 0.2				0.70 $\pm$ 0	157.7 $\pm$ 1.9	49.8 $\pm$ 1.7	0.94 $\pm$ 0	172.1 $\pm$ 0.7	41.6 $\pm$ 0.5	1.00 $\pm$ 0	186.2 $\pm$ 1.1	39.6 $\pm$ 0.8
	TD											
	MWTD	0.21 $\pm$ 0	107.4 $\pm$ 7.1	74.3 $\pm$ 20.7								
	the halo	0.79 $\pm$ 0.07	10.0 $\pm$ 6.9	77.2 $\pm$ 4.0	0.30 $\pm$ 0.02	7.0 $\pm$ 2.8	59.5 $\pm$ 3.0	0.06 $\pm$ 0.01	43.0 $\pm$ 5.5	43.0 $\pm$ 2.9		
< 0.2				0.56 $\pm$ 0	185.6 $\pm$ 4.2	40.9 $\pm$ 2.9	0.96 $\pm$ 0	191.9 $\pm$ 0.6	40.9 $\pm$ 0.5	1.00 $\pm$ 0	196.4 $\pm$ 0.5	36.1 $\pm$ 0.4
	TD											
	the halo			0.44 $\pm$ 0.04	27.2 $\pm$ 8.5	59.2 $\pm$ 6.4	0.04 $\pm$ 0	41.7 $\pm$ 5.1	48.9 $\pm$ 3.2			

MWTD has obvious contribution only in panel a of Fig. 6. The fraction of MWTD in this panel is 0.24, which is lower than that in the same panel of the inner region. The  $L_Z$  peak of MWTD in this panel is  $996.9 \pm 22.0 \text{ kpc km s}^{-1}$  with a scatter of  $687.8 \pm 62.1 \text{ kpc km s}^{-1}$ , and we note that this scatter is larger than that of the inner ones ( $\sim 500 \text{ kpc km s}^{-1}$ ). The reason is most likely due to the fraction of MWTD in the outer region is lower than that in the inner one.

### 3.2 The $V_\phi$ distributions

It is noted by An & Beers (2021), Carollo et al. (2010) and Kordopatis et al. (2013) that MWTD has kinematic properties different from those of the halo and TD, thus, we display the  $V_\phi$  distribution of the inner and outer region stars in Figs. 7 and 8 in slices of [Fe/H] and [ $\alpha$ /Fe], respectively. The best-fit result obtained with the MCMC simulation are superimposed on the histogram with color curves, and the best-fit parameters are listed in Tables 3 and 4.

In each panel of the two figures (Figs. 7 and 8), the components determined from the  $V_\phi$  distribution are very similar to those from the  $L_Z$  ones. The  $V_\phi$  peak of MWTD in the panels a and b of the inner region are  $124.9 \pm 6.3 \text{ km s}^{-1}$  and  $117.8 \pm 10.7 \text{ km s}^{-1}$ , respectively, while it is  $107.4 \pm 7.1 \text{ km s}^{-1}$  in the panel a of the outer region, which are consistent with those of Carollo et al. (2010) and Kordopatis et al. (2013), however, they are around  $15 \text{ km s}^{-1}$  lower than those of An & Beers (2021). We note that the metallicities for the sample stars of An & Beers (2021) were estimated from the photometric data, while the  $V_\phi$  of their individual stars were computed using photometric distances and proper-motion measure-

ments from Gaia EDR3, and their sample restrict to stars within  $\pm 30^\circ$  from the Galactic prime meridian. Therefore, the difference in  $V_\phi$  may due to the different in sample stars.

#### 4 DISCUSSION AND CONCLUSIONS

Based on the combined dataset of LAMOST DR5 and Gaia EDR3, we investigate the kinematic properties of the giant stars in the solar neighbourhood. Our results show that MWTD occupies a significantly fraction with metallicity lower than  $-0.8$  and  $[\alpha/\text{Fe}] > +0.2$  dex. It is found that the fraction of MWTD is significantly higher within the solar orbit radius, while the Z-axis angular momentum is similar for both subsamples divided by the solar orbit radius,  $950$  and  $1000 \text{ kpc km s}^{-1}$  for inner and outer region, respectively. The high fraction of MWTD in the inner solar orbit radius and higher  $\alpha$  element abundances may suggest that the MWTD stars were born in the inner region of the primordial disk, and some of them migrated to larger radii, or MWTD is the result of inside out scenario. However, the number of the MWTD stars is relatively small compared to the TD and halo ones, thus, it is hard to make an ascertained estimation of the origin of MWTD under the current situations. To figure out the origin of MWTD, additional constraints from both **observations** (such as the abundances of C, N, O, Mg, Si, Ca and Ti, etc) and numerical simulations are necessary.

#### ACKNOWLEDGEMENTS

Our research is supported by National Key R&D Program of China No.2019YFA0405500, the National Natural Science Foundation of China under grant Nos. 12090040, 12090044, 11833006, 12022304, 11973052, 11973042, 1214028, U2031143 and U1931102. This work is supported by the Astronomical Big Data Joint Research Center, co-founded by the National Astronomical Observatories, Chinese Academy of Sciences and Alibaba Cloud. This work is also partially supported by the Open Project Program of the Key Laboratory of Optical Astronomy, National Astronomical Observatories, Chinese Academy of Sciences. Guoshoujing Telescope (the Large Sky Area Multi-Object Fiber Spectroscopic Telescope LAMOST) is a National Major Scientific Project built by the Chinese Academy of Sciences. Funding for the project has been provided by the National Development and Reform Commission. LAMOST is operated and managed by the National Astronomical Observatories, Chinese Academy of Sciences. This work has made use of data from the European Space Agency (ESA) mission Gaia (<https://www.cosmos.esa.int/gaia>), processed by the Gaia Data Processing and Analysis Consortium (DPAC, <https://www.cosmos.esa.int/web/gaia/dpac/consortium>). Funding for the DPAC has been provided by national institutions, in particular the institutions participating in the Gaia Multilateral Agreement.

#### References

- An, D., & Beers, T. C. 2020, *ApJ*, 897, 39  
 An, D., & Beers, T. C. 2021, *ApJ*, 918, 74  
 Anguiano, B., Majewski, S. R., Allende-Prieto, C., et al. 2018, *A&A*, 620, A76  
 Bailer-Jones, C. A. L., Rybizki, J., Fouesneau, M., et al. 2021, *AJ*, 161, 147  
 Beers, T. C., Norris, J. E., Placco, V. M., et al. 2014, *ApJ*, 794, 58  
 Beraldo e Silva, L., Debattista, V. P., Nidever, D., et al. 2021, *MNRAS*, 502, 260  
 Carollo, D., Beers, T. C., Chiba, M., et al. 2010, *ApJ*, 712, 692  
 Carollo, D., Chiba, M., Ishigaki, M., et al. 2019, *ApJ*, 887, 22  
 Carollo, D., & Chiba, M. 2020, arXiv:2010.00235  
 Chiappini, C., Matteucci, F., & Gratton, G. 1997, *ApJ*, 477, 765  
 Chiba, M., & Beers, T. C. 2000, *AJ*, 119, 2843  
 Cordoni, G., Da Costa, G. S., Yong, D., et al. 2021, *MNRAS*, 503, 2539  
 Cui, X. -Q., Zhao, Y. -H., Chu, Y. -Q., et al. 2012, *RAA*, 9, 1197  
 Di Matteo, P., Lehnert, M. D., Qu, -Y., & van Driel, W. 2011, *A&A*, 525, L3

- Di Matteo, P., Fragkoudi, F., Khoperskov, S., et al. 2019, *A&A*, 628, A11
- Foreman-Mackey, D., Hogg, D. W., Lang, D., & Goodman, J. 2013, *PASP*, 125, 306
- Franchini, M., Morossi, C., Di Marcantonio, P., et al. 2021, *AJ*, 161, 9
- Gaia Collaboration., Brown, A. G. A., Vallenari, A., et al. 2021, *A&A*, 649, A1
- Gilmore, G., & Reid, N. 1983, *MNRAS*, 202, 1025
- Girard, T. M., Korhagin, V. I., Casetti-Dinescu, D. I., & van Altena, W. F. 2006, *AJ*, 132, 1768
- Hayden, M. R., Holtzmann, J. A., Bovy, J., et al. 2014, *AJ*, 147, 116
- Helmi, A., Babusiaux, C., Koppelman, H. H., et al. 2018, *Nature*, 563, 85
- Ivezić, Ž., Sesar, B., Juriić, M., et al. 2008, *ApJ*, 684, 287
- Kordopatis, G., Recio-Blanco, A., de Laverny, P., et al. 2011, *A&A*, 535, A107
- Kordopatis, G., Gilmore, G., Wyse, R.F.G., et al. 2013, *MNRAS*, 436, 3231
- Luo, A. -L., Zhao, Y. -H., Zhao, G., et al. 2015, *RAA*, 15, 1095
- Miranda, R., Pilkington, K., Gibson, B. K., et al. 2016, *A&A*, 587, A10
- Morrison, H. L., Flynn, C., & Freeman, K. C. 1990, *AJ*, 100, 1191
- Naidu, R. P., Conroy, C., Vonaca, A., et al. 2020, *ApJ*, 901, 48
- Norris, J., Bessell, M. S., & Pickles, A. J. 1985, *ApJS*, 58, 463
- Recio-Blanco, A., de Laverny, P., Kordopatis, G., et al. 2014, *A&A*, 567, A5
- Reddy, B. E., & Lambert, D. L. 2008, *MNRAS*, 391, 95
- Reid, M. J., Menten, K. M., Brunthaler, A., et al. 2014, *ApJ*, 783, 130
- Ruchti, G. R., Fulbright, J. P., Wyse, R. F. G., et al. 2010, *ApJ*, 721, 92
- Ruchti, G. R., Fulbright, J. P., Wyse, R. F. G., et al. 2011, *ApJ*, 737, 9
- Ryan, S. G., & Lambert, D. L. 1995, *AJ*, 109, 2068
- Schönrich, R., Binney, J. & Dehnen, W. 2010, *MNRAS*, 403, 1829
- Steinmetz, M., Matijević, G., Enke, H., et al. 2020a, *AJ*, 160, 82
- Steinmetz, M., Guiglion, G., McMillan, P. J., et al. 2020b, *AJ*, 160, 83
- Tian, H., Liu, C., Xu, Y., & Xue, X. -X. 2019, *ApJ*, 871, 184
- Tian, H., Liu, C., Wang, Y. -G., et al. 2020, *ApJ*, 899, 110
- Twarog, B. A., & Anthony-Twarog, B. J. 1994, *AJ*, 107, 1371
- van der Kruit, P. C., & Freeman, F. C. 2011, *ARA&A*, 49, 301
- Xiang, M. -S., Ting, Y. -S., Rix, H.-W, et al. 2019, *ApJS*, 245, 34
- York, D. G., Adelman, J., Anderson, J. E., et al. 2000, *AJ*, 120, 1579



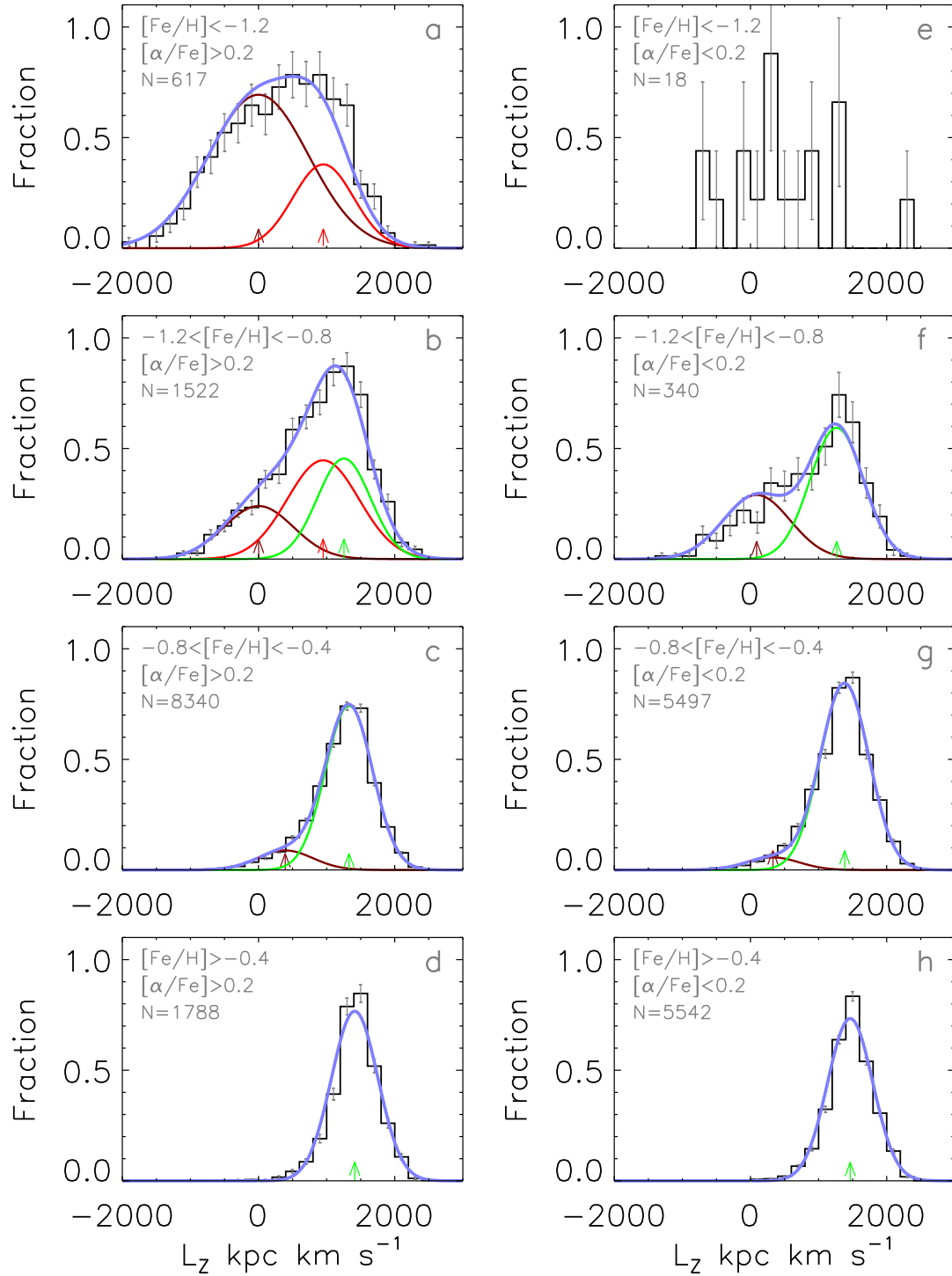


Fig. 4: The  $L_Z$  distributions of the inner region stars in slices of  $[\text{Fe}/\text{H}]$  and  $[\alpha/\text{Fe}]$ . The distribution can be best-fitted by one to three Gaussian(s), and each represents one component: the halo (brown), MWTD (red) and TD (green). The black histogram is the sum of all stars, while the light blue solid line represents the sum of the fit components.

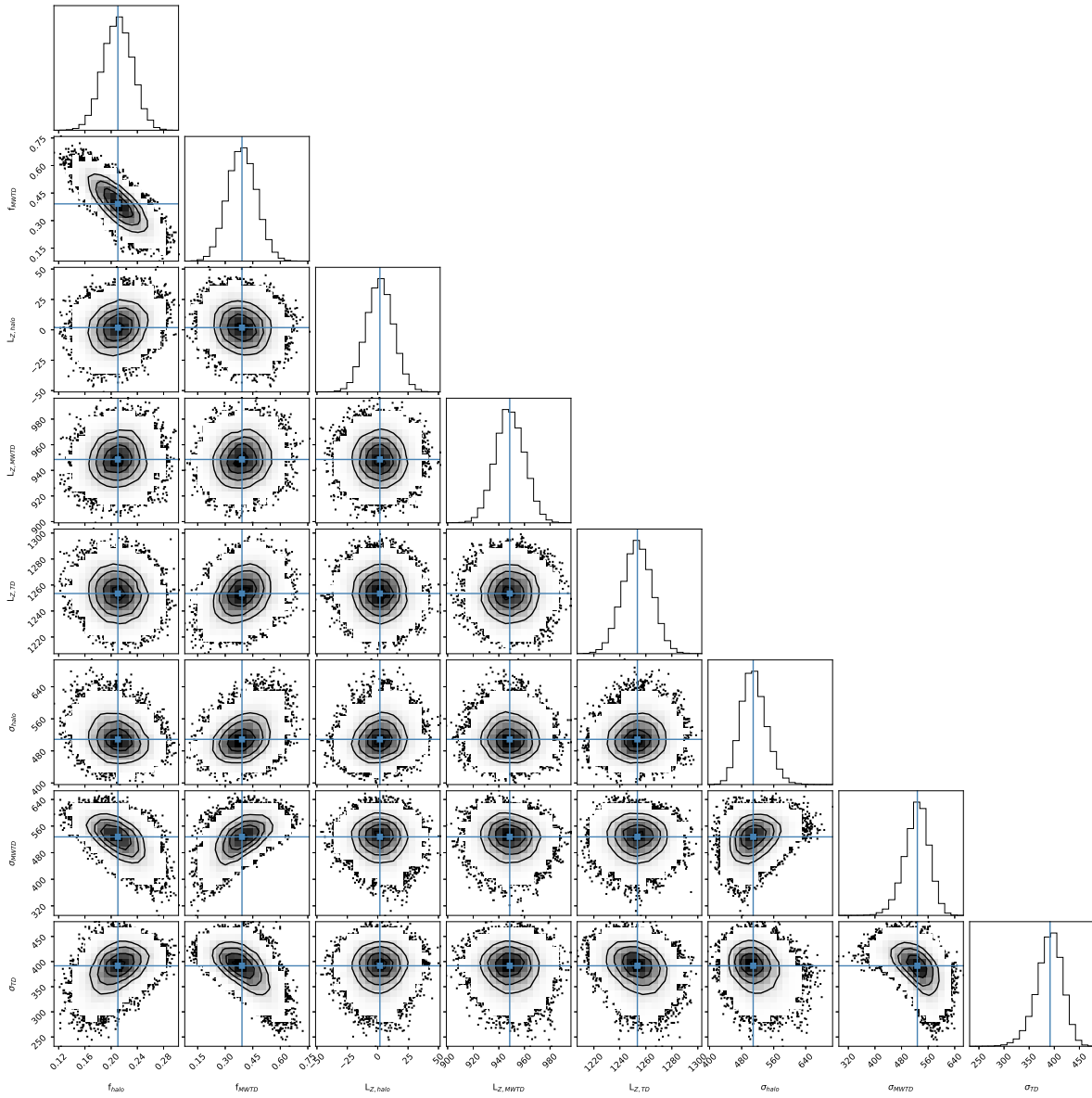


Fig. 5: The MCMC simulation results of the panel b of Fig. 4. The adopted median values of the parameters are represented by the solid blue lines.

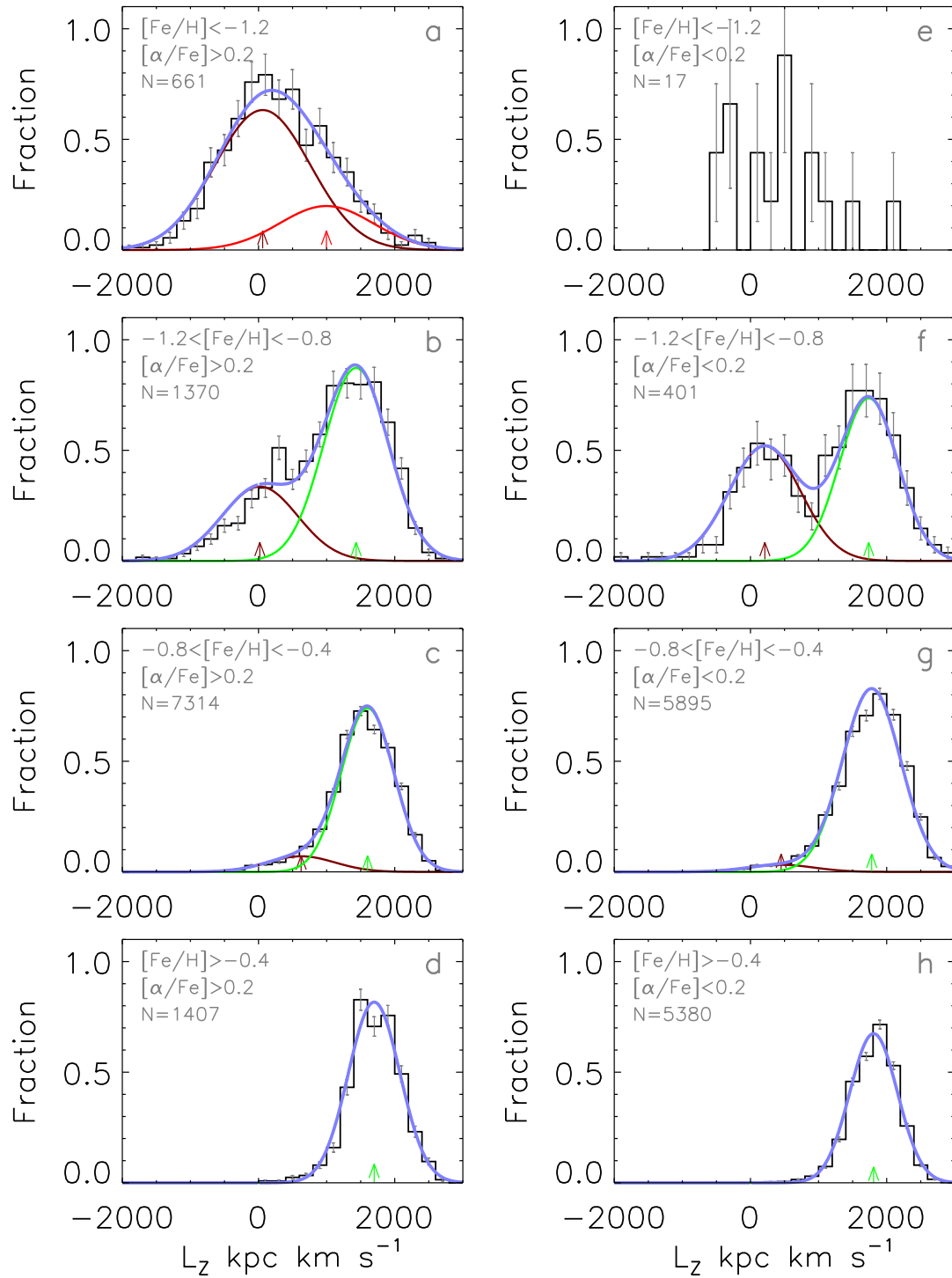


Fig. 6: Similar to Fig. 4 but for the  $L_z$  Distribution of outer region stars.

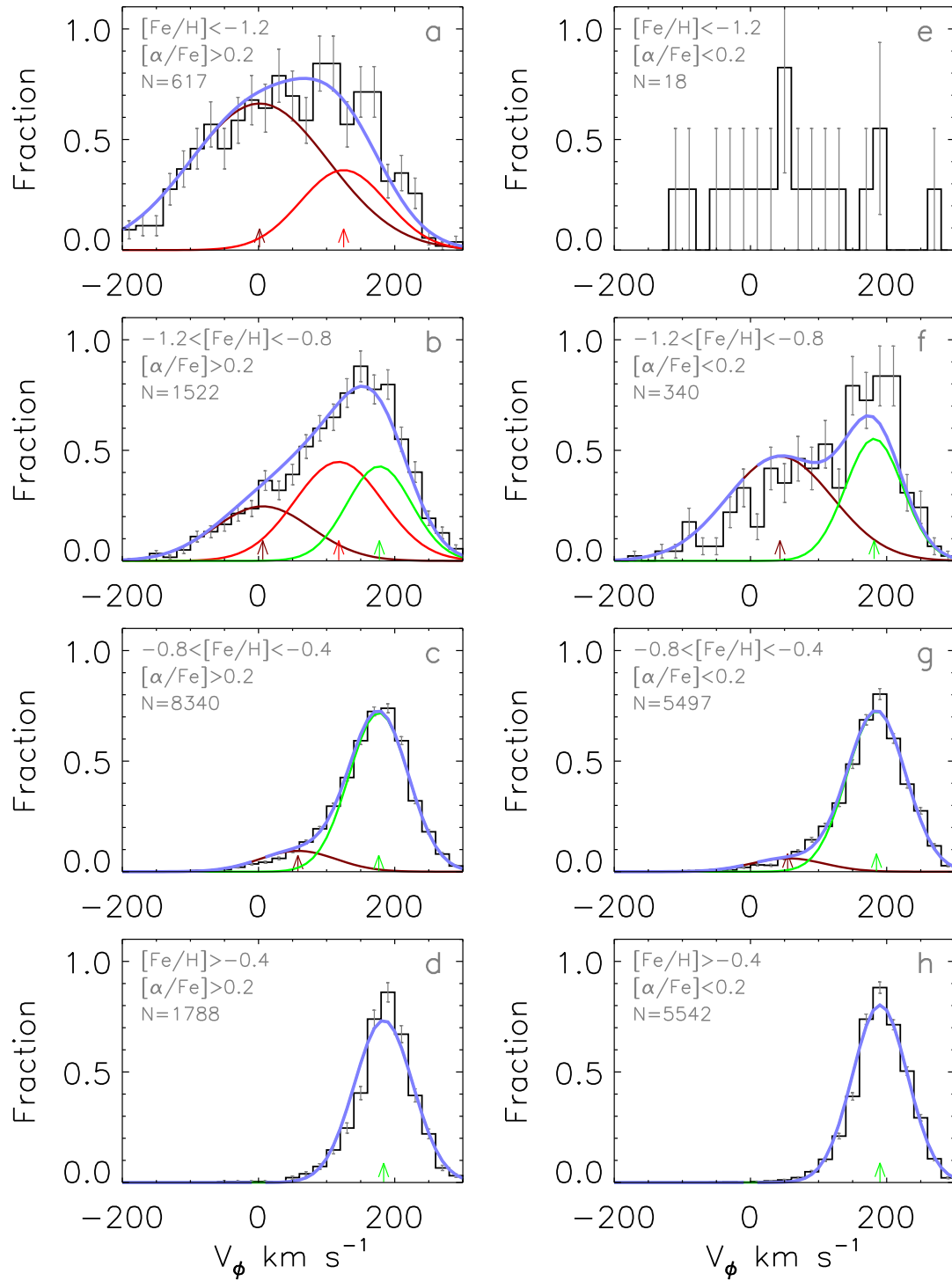
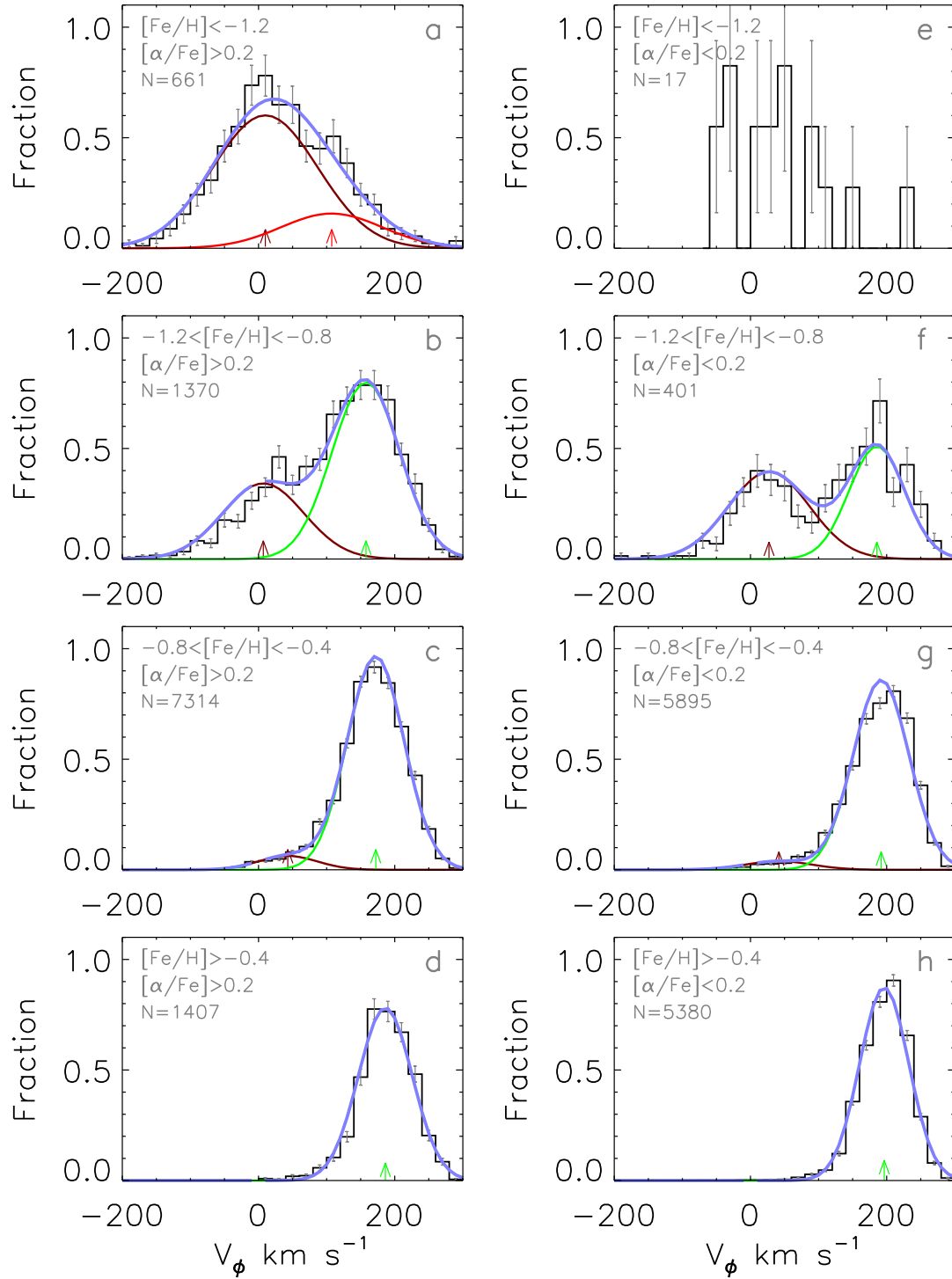


Fig. 7: Similar to Fig. 4 but for the  $V_\phi$  distribution.

Fig. 8: Similar to Fig. 7 but for the outer stars ( $R_{GC} > 8.34$  kpc).